Wu, Chenchen; Guo, Xiangdong; Duan, Yu; Lyu, Wei; Hu, Hai; Hu, Debo; Chen, Ke; Sun, Zhipei; Gao, Teng; Yang, Xiaoxia; Dai, Qing

Ultrasensitive Mid-Infrared Biosensing in Aqueous Solutions with Graphene Plasmons

Published in:
Advanced Materials

DOI:
10.1002/adma.202110525

Published: 07/07/2022

Document Version
Peer-reviewed accepted author manuscript, also known as Final accepted manuscript or Post-print

Please cite the original version:
Wu, C., Guo, X., Duan, Y., Lyu, W., Hu, H., Hu, D., Chen, K., Sun, Z., Gao, T., Yang, X., & Dai, Q. (2022). Ultrasensitive Mid-Infrared Biosensing in Aqueous Solutions with Graphene Plasmons. *Advanced Materials*, *34*(27), Article 2110525. https://doi.org/10.1002/adma.202110525

Ultrasensitive Mid-Infrared Biosensing in Aqueous Solutions with Graphene Plasmons

Chenchen Wu[1,2], Xiangdong Guo[1,2], Yu Duan[1], Wei Lyu[1], Hai Hu[1,2], Debo Hu[1,2], Ke Chen[1,2], Zhipei Sun[3], Teng Gao[1], Xiaoxia Yang[1,2]* and Qing Dai[1,2]*

[1]CAS Key Laboratory of Nanophotonic Materials and Devices, CAS Key Laboratory of Standardization and Measurement for Nanotechnology, CAS Center for Excellence in Nanoscience, National Center for Nanoscience and Technology, Beijing 100190, China

[2]Center of Materials Science and Optoelectronics Engineering, University of Chinese Academy of Sciences, Beijing 100049, China

[3]Department of Electronics and Nanoengineering and QTF Centre of Excellence, Department of Applied Physics, Aalto University, Espoo 02150, Finland.

* *Corresponding authors:* daiq@nanoctr.cn, yangxx@nanoctr.cn

Abstract

Identifying biomolecules in aqueous solutions by Fourier transform infrared spectroscopy (FTIR) provides an in-situ and non-invasive method for exploring the structure, reactions, and transport of biologically active molecules. However, the strong and broad infrared (IR) absorption band of water molecules overwhelms the respective vibrational fingerprints of the biomolecules. Along these lines, we exploit the tunable graphene plasmons to identify ~2 nm protein molecules in physiological conditions. More specifically, the ultrahigh confinement effect of graphene plasmons (confined to ~15 nm) minimizes the environmental noise and permits the implementation of nanoscale sensitivity. Most importantly, the acquired dynamic tunability eliminates the impact of the water IR absorption outside the graphene plasmonic hotspots and renders the selective probe of the protein vibrations at different frequencies. Therefore, the deuterium effects on monolayer proteins are characterized within an aqueous solution. Additionally, the proposed tunable graphene plasmon-enhanced FTIR technology provides a novel platform for the in-situ identification of biologically active molecules in an aqueous solution at the nanoscale.

Keywords: graphene plasmons, surface-enhanced infrared spectroscopy, biosensing, aqueous solutions

Introduction

The length scale of a biomolecule is usually in a few nanometers.[1] For instance, proteins that are considered the most complex nanoscale molecular machines are found within cells, whereas the biomolecular corona interface composition, the host-pathogen recognition interactions, and the nanomedicine targeting effects also happen at the nanoscale level.[2-4] Thus, it is important to develop in-situ and nondestructive methods with nanoscale resolutions to understand biological processes in physiological environments.[5-7] Along these lines, Fourier transform infrared spectroscopy (FTIR) serves as a label-free, non-invasive, and fast method for identifying biomolecules by detecting their individual molecular vibrational fingerprints.[8] However, achieving aqueous FTIR with nanoscale sensitivity remains a challenge since the broad and strong infrared (IR) band of water (H_2O) always masks the vibrational fingerprints of the biomolecules, especially in the mid-IR range.[9,10]

To implement the vibrational fingerprints masked by H_2O, deuterium oxide (D_2O) is used for aqueous samples in FTIR measurements, since its IR absorption band is shifted away from H_2O absorption band. However, the abnormal structure and function expression of biomolecules induced by the presence of D_2O prevents the in-situ study of bioactivities.[11,12] Another potential route is to shorten the effective IR optical path in an aqueous solution in order to suppress the interference of H_2O, such as the attenuated total reflectance (ATR).[13,14] Nevertheless, neither solvent replacement nor ATR can enhance nanoscale sensitivity for the limited FTIR instrumental detection sensitivity. Therefore, the surface-enhanced infrared spectroscopy (SEIRA) technique was developed for in-situ probing nanoscale samples through the evanescent field of the surface plasmons that are directly associated with the inner reflection process.[9,15-17] Although the metal plasmon-enhanced FTIR effect has already achieved high sensitivity, the detection limit is ultimately restricted to monolayer molecules by the relatively poor light confinement of the metal in the mid-IR.

The extreme light confinement effect with graphene plasmon renders it attractive for SEIRA applications. Interestingly to notice that the sensitivity of graphene plasmon-enhanced FTIR can be enhanced to the sub-nanometer scale, which has been previously applied on identifying molecules in the solid phase[18-21] and gas phase[22]. Graphene plasmon has also been employed to increase the sensitivity of the aqueous FTIR via the

inner reflection process[23,24], but the lack of tunability, as well as the utilization of bulky ATR instrumentation, have prevented it from practical use[25].

In this work, we developed a tunable graphene plasmon-enhanced FTIR technology to identify nanoscale proteins in physiological conditions. This effect was attained by eliminating the noise constituted by strong water absorption outside the graphene IR plasmon hotspots via enforcing an in-situ background subtracting method in FTIR measurements by external electrical gating. As a result, a nanoscale sensitivity with ~2 nm thickness of protein molecules was demonstrated due to the highly confined electromagnetic field distribution of the graphene plasmon (~15 nm for 90% mode energy confinement)[18]. Moreover, the reported lowest detection limit in aqueous solutions (~2 nm) enabled by our approach, in turn, allows the direct monitoring of the protein hydrogen(H)/deuterium(D) exchange process within an aqueous solution by performing FTIR transmission measurements.

Results and Discussion

The tunable graphene plasmon-enhanced FTIR platform for protein identification

The proposed tunable graphene plasmonic aqueous IR (GP-aIR) biosensor is schematically illustrated in Fig. 1a. As can be ascertained, it is composed of a graphene plasmonic device and an IR transparent microfluidic system (more details in Methods and Supplementary Fig. S1). We have to underline that the high IR transmittance is the foundation for the implementation of aqueous graphene plasmon-enhanced FTIR measurements. To achieve high IR transparency in aqueous FTIR measurements, a 200 μm thick calcium fluoride (CaF_2) crystal was chosen as the top window, whereas an atomically thin SiO_2/Si substrate supporting graphene devices as the bottom window of the microfluidic chamber. More importantly, the height of the microfluidic chamber at the graphene nanoribbon region (100 μm × 200 μm) was designed to be less than 5 μm for ensuring the steady flowing of the solution, as well as a high IR transparency for the FTIR measurements. As a result, the IR absorbance of this microfluidic chamber in the graphene nanoribbon region was less than 0.6 after filling with a protein solution (the blue curve in Fig. 1b).

To excite mid-IR plasmons, the graphene on the substrate was patterned to nanoribbon arrays with widths between 50 nm and 100 nm by enforcing the electron beam lithography and the oxygen plasma etching techniques (details in Methods and Supplementary Fig. S2). Consequently, a pair of gold electrodes with a titanium adhesion layer was evaporated on graphene as the source and drain contacts, whereas another electrode was evaporated outside graphene to play the role of the gate contact. The sub-nanometer thin electric double layer (EDL) formed on graphene and gold electrodes in the protein solution, works as a dielectric layer of the capacitor so that the graphene Fermi level can be modulated by varying gate based on the parallel plate capacitor theory. On top of that, a 200 nm thick PMMA film as the passivation layer was coated on the source and drain electrodes for preventing the direct interaction of the electrode materials with the aqueous solution and minimizing the current leakage. The extinction spectra were obtained by modulating the gate voltage, i.e., $1\text{-}T_{EF}/T_0$, where T_{EF} is the transmittance measured at a specific graphene Fermi level (*EF*), whereas T_0 is measured at the graphene charge neutral point (CNP). In addition, there is no graphene plasmon excited at CNP, and we employed the T_0 measured at this condition as a background signal for the FTIR measurement. Then, graphene nanoribbons were also doped by external gating to excite graphene plasmons, while we consequently measured the extinction spectrum as $1\text{-}T_{EF}/T_0$, which is the plasmonic response of the biosensor system. Thus, the background signal outside the plasmonic hotspot region was eliminated.

The red curve in Fig. 1b depicts a typical extinction spectrum as measured with 5 mg/ml protein solution after flowing for 1 hour. It is interesting to notice that two sharp dips at the wavenumbers of 1545 cm^{-1} (marked with green line) and 1655 cm^{-1} (marked with purple line) on the broad graphene plasmonic resonance peak can be detected. This effect is ascribed to the destructive interference of the graphene plasmon and the molecular vibrations. Therefore, the recorded dip at 1545 cm^{-1} can be identified as the amide II band, which is a typical protein molecular signature. However, the dip at 1655 cm^{-1} is at a region overlapped by the OH-bending mode of the water and amide I band of the protein. In order to shed light on these outcomes, we magnified the region between the wavenumber from 1600 cm^{-1} to 1700 cm^{-1}, and compared it with the respective graphene plasmon-enhanced extinction spectrum of the normal saline (as it is divulged in Fig. 1c). Without protein, the extinction spectrum of the saline solution

exhibits the water O-H bending mode at around 1645 cm^{-1} (the grey curve in Fig. 1c), while an 8 cm^{-1} shift to the 1655 cm^{-1} for the protein solution can also be recorded. Thus, we can assign the 1655 cm^{-1} dip to the amide I band other than the water OH-based bending mode.

Surprisingly, the signal strength of the protein exceeds that of water in the extinction spectrum, implying the existence of more protein molecules than water molecules in the plasmon hotspots on the graphene nanoribbons. By carrying out theoretical calculations (see Supplementary Fig. S3 and Note 1), we found that the density of the protein molecules is enriched by $\sim 3\times10^4$ times on the graphene nanoribbons compared with that of the protein solution. This result implies the protein adsorption on the graphene surface. It is well established from the literature that molecules are likely to be adsorbed on graphene by using several adsorption mechanisms, such as physisorption[22,26-28], optical trapping[29-31], and static dielectrophoretic forces[32-34]. By considering our previously reported theoretical calculations, the physisorption of molecules on graphene is regarded as the driving force, while the others are negligible.[27,35] More importantly, a hydrophobic-based graphene surface is more likely to adsorb the protein molecules with hydrophobic groups.[36] Furthermore, the enriched protein molecules on graphene nanoribbons are schematically revealed on the right of Fig. 1a. We have to underline that the electromagnetic field distribution is confined around the graphene nanoribbons due to the manifestation of the plasmonic resonances effects (illustrated as the red chamber shown in Fig. 1c). Therefore, as the protein molecules are adsorbed on the nanoribbon's structures, their IR absorptions are enhanced dramatically by the graphene plasmon. Thus, our tunable graphene plasmon-enhanced FTIR platform discloses superior sensitivity for the identification of proteins even in normal saline.

Additionally, the liquid gate via EDL permits the modulation of the graphene plasmons in a wide frequency range. More specifically, a typical transfer characteristic curve of the GP-aIR biosensor after the physisorption–based saturation of the protein molecules saturated in the aqueous solution is highlighted in Fig. 2a (blue line). The graphene Fermi energy can be calculated by applying a parallel plate capacitor model. The sub-nanometer thin electric double layer (EDL) is formed on both the graphene and gold electrodes in the protein solution, which operates via a liquid gate and has a higher modulation efficiency than the back-gate with the SiO_2 dielectric layer[37]. The

estimated liquid-gate capacitance of our GP-aIR biosensor in the protein solution is C_{top}~385 nF/cm^2 (see Supplementary Note 2), whereas the corresponding Fermi energy is depicted by the green curve in Fig. 2a.

Moreover, the extinction spectra of the GP-aIR biosensor at different Fermi levels are divulged in Fig. 2b. As can be ascertained, the plasmon resonance frequency is dynamically modulated from the value of ~1300 cm^{-1} to 1700 cm^{-1} when the Fermi level is adjusted from ~0.11 to 0.25 eV. More importantly, the coupling strength of the protein vibrational mode is enhanced as the detuning of the graphene plasmons and the molecular vibrational modes decrease, which is consistent with the acquired numerical calculation results (the dash curves in Fig. 2b). It is interesting to notice that when the resonance frequency of the graphene plasmons is shifted from ~1200 cm^{-1} to 1560 cm^{-1}, the coupling strength between graphene plasmon and amide II band is enhanced, while the dip at 1545 cm^{-1} is getting even deeper. With the further increase of the Fermi level at the value of 0.25 eV, the dip at the amide II band becomes shallower, whereas the dip at 1655 cm^{-1}gradually deepens due to the stronger coupling between the amide I band and graphene plasmon. Furthermore, the coupling mechanism between graphene plasmons and molecular vibrational modes can be described as a coupling process between two harmonic oscillators. Although the far-field incident IR light cannot efficiently drive the molecular vibration due to the significant size mismatch, the stronger oscillation properties of graphene plasmon can more efficiently drive the molecular vibration.[38,39] Therefore, it is possible to tune the graphene Fermi energy and realize selective plasmonic response in the mid-IR in order to identify protein vibrational fingerprints by enforcing different gate voltages.

Protein identification with ultralow detection limit

Here, we investigate the detection limit of the proposed GP-aIR biosensor by monitoring the adsorption process of protein on the graphene nanoribbons. When protein solution was injected into the GP-aIR biosensor, the protein molecules were gradually adsorbed on the graphene nanoribbons and finally reached a saturated state in 20 min. The extinction spectra of the GP-aIR biosensor, which were measured at different times during this process, are disclosed in Supplementary Fig. S4. To exhibit the plasmon-enhanced molecular signals more clearly, we extracted them from the plasmon resonance peaks in the as-measured extinction spectra, as demonstrated in Fig.

3a. At the beginning of injecting the protein solution (0 min), only one broad peak at around 1645 cm^{-1} can be recorded due to the OH-bending mode of the water. As the adsorption time becomes bigger (injecting the protein solution for 7 min, 8 min, 16 min, 20 min), the acquired IR response of the amide II band (~1545 cm^{-1}) appears and constantly enhances as indicated by a green arrow. The IR response near 1645 cm^{-1} is blue shifting to 1655 cm^{-1}, which can be identified as the amide I protein band (purple arrow).

To further understand this process, we performed finite-element method (FEM) simulations (see details in Methods and Supplementary Fig. S3). Interestingly, the obtained extinction spectra are in excellent agreement with the respective experimental spectra when considering the adsorbed protein layer with the following thickness values: 0 nm, 2 nm, 4 nm, 6 nm, and 8 nm (Fig. 3c). We have also to underline that the thickness of the protein layer is also consistent with the experimentally measured values. On top of that, we carried out atomic force microscopy (AFM) measurements on the graphene nanoribbons at different adsorption time. The GP-aIR biosensor taken out of the protein solution was washed with deionized water several times and dried in flowing nitrogen. As can be observed from Fig. 3b and Supplementary Fig. S5, the height of the graphene nanoribbons increases from ~2 nm to ~8 nm with increasing adsorption time, which verifies that protein molecules are gradually adsorbed on the graphene nanoribbons.

The acquired electrical response can also support the measured results of the proposed GP-aIR biosensor. The protein molecules are negatively charged in our protein solution since its pH value (about 7) is larger than the isoelectric point of the bovine serum albumin (BSA) protein (5.3)[37]. Thus, there are electrons transferred to graphene film after the protein adsorption procedure. The transfer characteristics of the GP-aIR biosensor were also measured at different times during the protein adsorption process to calculate the change of the CNP value extracted from the transfer characteristic curve (see Supplementary Fig. S5), which arises from the protein adsorption. As can be ascertained from Fig. 3d, the protein adsorption shifts the Fermi level of the graphene toward the Dirac point, while it changes fast at the beginning. Subsequently, the speed of the change becomes slow and finally reaches saturated adsorption ($\Delta E_F \sim 90$ meV). In order to exclude the n-doping effect of other ions in the protein solution[40-42], normal saline was first injected inside until the CNP of the GP-aIR biosensor stabilizes, and then the protein solution with the same NaCl concentration

as normal saline was injected. The change law and the time required for the saturated adsorption were displayed by the electrical results, which corroborated the outcomes of the GP-aIR biosensor.

More specifically, these results point out that the GP-aIR biosensor is sensitive to the presence of proteins in aqueous solution due to the high sensitivity of the graphene plasmons to the absorbed protein (obvious response for 2 nm protein), as well as to the adsorption of molecules on graphene. Thus, we measured a solution with different protein concentrations, and the outcomes of 100 pg/mL and 100 ng/mL solution are revealed in Supplementary Fig. S6. After flowing in the solution for 2 hours, both the amide I and amide II bands can be clearly detected by the GP-aIR biosensor.

Monitoring of protein molecules during a H/D exchange process

H/D exchange is widely used in exploring protein structures and functions for identifying and understanding the complex biological processes and developing pharmaceutical drugs[43-46]. The exposure of a protein to D_2O induces amide H/D exchange in disordered regions that lack stable hydrogen bonding. We have to underline that the tightly folded elements are much more protected from the H/D exchange resulting thus in slow isotope exchange.[47] The investigation of the interaction rate and sites of the H/D exchange between the amide hydrogens of the protein backbone and its surrounding solvent reflects not only the folded state of the protein and its dynamics but also the intrinsic chemical properties of the underlying amino acid sequence.[45] Nuclear magnetic resonance spectroscopy (NMR) is currently the most important method to characterize proteins in solution by analyzing the NMR signal of the nuclei of atoms in the protein, but it relies on expensive and complicated equipment and strict sample preparation. A fast and non-invasive method in order to directly monitor the proton exchange process in an aqueous solution is still missing.

Along these lines, we demonstrate that the tunable graphene plasmon-enhanced FTIR platform can directly monitor the H/D exchange mechanism of nanoscale protein molecules within an aqueous solution. Initially, the GP-aIR biosensor flows with a protein solution (solvent: H_2O water) for 1 hour for reaching saturated adsorption of the protein molecules on the graphene nanoribbons. Subsequently, D_2O was injected into the sensor cell for 0.5 hours in order to make sure a complete H/D exchange for the proteins. Then, H_2O and D_2O were alternately injected several times, while the

extinction spectra of graphene plasmon were measured (see Supplementary Fig. S7). For comparison, the plasmon-enhanced protein responses were extracted and disclosed in Fig. 4a. The most obvious change in the acquired spectra is that the peak corresponding to the amide II band shifts from 1545 cm^{-1} to 1457 cm^{-1} by replacing the H_2O with D_2O, and it recovers when reinjecting H_2O. We have to underline that according to the literature the 1457 cm^{-1} is assigned to the amide II of deuterated protein.[48] The amide II band arises from the coupling of the N-H/D bending and C-N stretching modes (Fig. 4b). As a result, the red shift of the amide II band provides direct evidence of the H/D exchange. Additionally, during this H/D exchange process, the amide I band (C=O stretching) of protein at 1655 cm^{-1} has a slight redshift, because hydrogen bonds effects vary on secondary structure in different solvents. It is interesting to notice that, due to the hygroscopicity of D_2O, there are also a small amount of H_2O in our D_2O since the measurements were taken under atmosphere conditions, as is demonstrated by the manifestation of the following bending modes in the IR spectrum of D_2O: H-O-D (1457 cm^{-1}), D-O-D (1212 cm^{-1}) and H-O-H (1645 cm^{-1}) (Supplementary Fig. S7a). Therefore, the peak at 1457 cm^{-1} may not only originate from the shifted amide II, but also from the H-O-D.

Furthermore, we investigated the H/D protein exchange process on the protein molecular structures in solution by employing different concentrations (17%, 34%, 51%, 68%, 85%) of D_2O. The extinction spectra of graphene plasmons-enhance the FTIR response at each concentration are collected (Supplementary S7), while the plasmonic enhanced signals are extracted and plotted in Fig. 4c. Compared with the respective extinction spectrum in H_2O, the coupling strength of both the amide I band (around 1655 cm^{-1}) and the amide II band (around 1545 cm^{-1}) decreases by increasing the D_2O concentration. On top of that, the ratio of H/D exchange is consistent with the concentration of heavy water, indicating that within the nanoscale protein, the H/D exchange process occurs with high efficiency and reaches a dynamic equilibrium at a high concentration level of D_2O, because nanoscale proteins have a larger proportion of surface structures that exposed to the environment. From this outcome, we can conclude that our approach exhibits high detection sensitivity and can monitor the proton exchange process of nanoscale-based proteins.

Discussion

In conclusion, we adapted graphene plasmons to identify nanoscale protein fingerprints in physiological conditions by employing a tunable graphene plasmon-enhanced FTIR platform. The induced graphene plasmons can essentially enhance the light-matter interaction and push the sensitivity down to the value of 2 nm thickness which is the highest reported sensitivity of the aqueous FTIR. More specifically, the protein fingerprints identification within the aqueous solution is achieved due to the highly confined optical field and tunability of the graphene plasmons. Meanwhile, we exhibit the dynamic and reversible H/D exchange on the protein molecular structure with the assistance of the GP-aIR biosensor. Interestingly, D_2O was found to affect the nanoscale proteins structures by hydrogen bonds effects on secondary structure and NH/ND exchange on the amide bonds. The exciting performance of our approach paves the way for the implementation of an in-situ studying bioprocess within complex physiological environments with ultralow detection limit, which provides a new strategy for studying the nano-bio interface and opens an inspiring outlook for both nanotoxicology and nano pharmacology.

Methods

Aqueous graphene plasmonic IR biosensor

The proposed graphene plasmonic device is composed of connected graphene nanoribbon arrays patterned on a SiO_2/Si substrate by employing electron beam lithography and oxygen plasma etching techniques. Then it is well encapsulated with the microfluidic system by utilizing O rings made by nitrile butadiene. The single graphene layer was grown on copper foil by chemical vapor deposition method and consequently was transferred to a 285 nm SiO_2/500 μm SiO_2 substrate using the wet transfer method. The graphene film is of high quality and continuous, as it was confirmed by the optical image (Supplementary Fig. S2a), the scanning electron microscope image (Supplementary Fig. S2b), and the Raman spectra (Supplementary Fig. S2c). The carrier mobility of the graphene is ~900 $cm^2/(V*s)$, which is extracted from the transfer characteristic curve of the aGP-IR biosensor. Next, a polymethyl methacrylate (950 K) film was spin-coated onto the sample. The nanoribbon arrays were patterned in graphene by using electron-beam lithography (Vistec 5000+ES, Germany) and then etched with oxygen plasma (SENTECH, Germany). The electrodes (5 nm Ti and 50 nm Au) were patterned and evaporated using electron-beam

lithography combined with electron beam evaporation (OHMIKER-50B, Taiwan). Moreover, the in-situ IR microfluidic system was custom-made from Zeptools Co. The thickness of the microfluidic chamber at the graphene nanoribbon region (100 μm * 200 μm) was designed to be less than 10 μm controlled by a gold spacer. In comparison, the thickness of the remaining region was 200 μm fabricated by photolithography (SUSS Ma-6, Germany) and deep reactive ion etching (Oxford Plasmalab System 100 ICP 180, England).

Characterization of the graphene plasmon devices.

The morphologies and thicknesses of the fabricated graphene nanoribbons were characterized by employing scanning electron microscopy (NOVA Nano SEM 430) and atomic force microscopy (Bruker ICON2-SYS) measurements. As far as the quality of the graphene and defect density of the nanoribbons are concerned, they were measured by Raman spectroscopy (Horiba Jobin Yvon LabRAM HR800) with laser excitation at 514 nm, laser power is 10%, and laser beam spot is ~1 μm. The electrical properties were determined by using a source meter (Keithley 2636B). In addition, FTIR transmission measurements were performed with Thermo Fisher Nicolet iN10 with an IR microscope (10x objective). The aperture was set as 100 μm*200 μm for each measurement, while the resolution was 8 cm^{-1} and scans were 128. The extinction spectra in this work were calculated with the following equation: Extinction=1-T_{EF}/T_0, where T_{EF} is the transmittance of graphene plasmons at certain fermi levels, and T_0 is the transmittance of the sensor at the graphene charge neutral point (CNP). The volume required to fill the liquid cell and permit the steady flow was approximately 0.1 mL, measured by filling with a syringe pump. The chamber was filled with a protein solution for static measurements, whereas the inlet and outlets were sealed to prevent flow. During the flowing measurements, a constant flow rate of 0.0083 $mL{\cdot}min^{-1}$ was maintained. The Keithley 2636B sourcemeter was also employed in order to tune the top gate voltage.

Near-Field Optical Microscopy Measurements.

Near-field imagining was conducted by using a commercially available s-SNOM (Neaspec GmbH), equipped with IR lasers (890-1700 cm^{-1}). The P-polarized IR light from the monochromatic quantum cascade lasers was focused via a parabolic mirror onto both the tip and sample at an angle of 60° to the surface normal. The probes were

made initially for metalized atomic force microscope (AFM) with an apex radius of ≈ 20 nm (Nanoworld).

Electromagnetic simulations and theory.

The electromagnetic simulations were conducted by using the commercial field solver, COMSOL Multiphysics. The graphene optical response was described via the Drude model. The employed protein solution parameters, including oscillator strength to each FTIR peak, were extracted, and fit the BSA film's measured IR absorbance. The simulation results were calculated by constructing a model utilizing a finite element electromagnetic simulation method. The graphene nanoribbon was modeled as a material with finite thickness and an equivalent relative permittivity distribution that depends on the thickness. The equal relative permittivity ε_g was derived from the surface conductivity σ of the graphene, calculated by the following expression: $\varepsilon_g = 1 + i\sigma/\varepsilon_0\omega t_g$, where ε_0 is the permittivity of the free space, ω is the angular frequency of the incident light and t_g is the graphene layer thickness. The graphene was modeled as a thin film and treated as the transition boundary condition with a thickness of just 0.34 nm. At room temperature (T = 300 K), the graphene surface conductivity can be approximately calculated from the Drude model:[49,50]

$$\sigma = \frac{ie^2 EF}{\pi\hbar^2(\omega + i/\tau)}$$

e is the electron charge, $\hbar$ is the reduced Planck constant, and EF is the Fermi energy of graphene. The relaxation time $\tau = \mu * EF/e\nu_F$, where ν_F =1×10^6 m/s is the Fermi velocity, and μ ~900 cm^2/(V*s) is the carrier mobility that extracted from experimental results.

The protein permittivity was retrieved from the experimental results by adjusting a Lorentzian permittivity[17,18]:

$$\varepsilon_{protein} = \varepsilon_\infty + \sum_{j=1}^{2} \frac{S_k^2}{\omega_j^2 - \omega^2 - i\Gamma_j\omega}$$

The extracted protein permittivity parameters from the experimental protein IR spectrum are: ε_∞=2.08, ω_1=1655 cm^{-1}, ω_2=1545 cm^{-1}, S_1=213 cm^{-1}, S_2=124 cm^{-1}, Γ_1=55.6 cm^{-1}, Γ_1=62 cm^{-1}. The simulation outcomes are in good agreement with the experimental absorption data. In the protein solution, the water IR absorption signal is

much stronger than protein molecules. Assuming that a monolayer protein is adsorbed on the graphene surface and considering the field contribution of the graphene plasmons, a protein layer with a thickness of 8 nm and a water layer with a thickness of 50 nm was utilized in the model for simplifying the calculation.

The chemicals sampling

The normal saline is 0.9% NaCl solution was prepared by dissolving NaCl (purity larger than 99.5%) in deionized water with a 100 mL volumetric flask. Moreover, the protein solution was prepared by dissolving bovine serum albumin (from KEH, Biotechnology Grade) in normal saline. D_2O was purchased from Macklin with 99.9 atom % D.

Data availability

The data that support the findings of this study are included with the manuscript as Supplementary Information. Any other relevant data are also available from the corresponding author upon reasonable request.

Acknowledgements

This work was supported by the National Natural Science Foundation of China (51925203, 52022025, 52102160, 51972074, 11674073, and U2032206), the Key Program of the Bureau of Frontier Sciences and Education, Chinese Academy of Sciences (QYZDB-SSW-SLH021), the Strategic Priority Research Program of the Chinese Academy of Sciences (XDB30000000 and XDB36000000), the Key Research Program of the Chinese Academy of Sciences (ZDBS-SSW-JSC002), Youth Innovation Promotion Association C.A.S., C.A.S. Interdisciplinary Innovation Team (JCTD-2018-03), and Academy of Finland (314810, 333982, 336144 and 336818), the Academy of Finland Flagship Programme (320167,PREIN), the European Union's Horizon 2020 research and innovation program (820423,S2QUIP; 965124, FEMTOCHIP), the EU H2020-MSCA-RISE-872049 (IPN-Bio), The Business Finland (ALDEL), and ERC (834742).

Author contributions

The concept for the experiment was initially developed by Q.D. and X.Y. FTIR experiments were performed by C.W. assisted by Y.D., W.L., H.H. and K.C., and FEM simulations and theoretical analysis were performed by C.W. and X.G. assisted by X.Y., D.H. Data processing and analysis were performed by C.W. assisted by Q.D., X.Y., Z.S. and T.G. C.W. wrote the manuscript with input from Q.D., X.Y. and Z.S. All authors discussed the results at all stages and participated in the development of the manuscript.

Additional information

Supplementary information is available in the online version of the paper. Reprints and permissions information is available online at www.nature.com/reprints. Publisher's note: Springer Nature remains neutral with regard to jurisdictional claims in published maps and institutional affiliations. Correspondence and requests for materials should

be addressed to Q.D. or X.Y.

Competing financial interests

The authors declare no competing financial interests.

Reference

1. Dawson, K.A. & Yan, Y. Current understanding of biological identity at the nanoscale and future prospects. *Nat. Nanotech.* **16**, 229-242 (2021).
2. Monopoli, M.P., Åberg, C., Salvati, A. & Dawson, K.A. Biomolecular coronas provide the biological identity of nanosized materials. *Nat. Nanotech.* **7**, 779-786 (2012).
3. Schöttler, S. et al. Protein adsorption is required for stealth effect of poly(ethylene glycol)- and poly(phosphoester)-coated nanocarriers. *Nat. Nanotech.* **11**, 372-377 (2016).
4. Kelly, P.M. et al. Mapping protein binding sites on the biomolecular corona of nanoparticles. *Nat. Nanotech.* **10**, 472-479 (2015).
5. Gomes, B.S., Simões, B. & Mendes, P.M. The increasing dynamic, functional complexity of bio-interface materials. *Nat. Rev. Chem* **2**, 0120 (2018).
6. Tenzer, S. et al. Rapid formation of plasma protein corona critically affects nanoparticle pathophysiology. *Nat. Nanotech.* **8**, 772-781 (2013).
7. Chen, F. et al. Complement proteins bind to nanoparticle protein corona and undergo dynamic exchange in vivo. *Nat. Nanotech.* **12**, 387-393 (2017).
8. Stuart, B.H. *Infrared spectroscopy: fundamentals and applications*, (John Wiley & Sons, 2004).
9. Etezadi, D., Warner, J.B.t., Lashuel, H.A. & Altug, H. Real-Time In Situ Secondary Structure Analysis of Protein Monolayer with Mid-Infrared Plasmonic Nanoantennas. *ACS Sens.* **3**, 1109-1117 (2018).
10. Pupeza, I. et al. Field-resolved infrared spectroscopy of biological systems. *Nature* **577**, 52-59 (2020).
11. Yang, H. et al. Obtaining information about protein secondary structures in aqueous solution using Fourier transform IR spectroscopy. *Nat. Protoc.* **10**, 382-396 (2015).
12. Makhatadze, G.I., Clore, G.M. & Gronenborn, A.M. Solvent isotope effect and protein stability. *Nature Struct. Biol.* **2**, 852-855 (1995).
13. Goulden, J.D.S. & Manning, D.J. Infra-red Spectra of Aqueous Solutions by the Attenuated Total Reflectance Technique. *Nature* **203**, 403-403 (1964).
14. Lu, R. et al. High-sensitivity infrared attenuated total reflectance sensors for in situ multicomponent detection of volatile organic compounds in water. *Nat. Protoc.* **11**, 377-386 (2016).
15. Adato, R. & Altug, H. In-situ ultra-sensitive infrared absorption spectroscopy of biomolecule interactions in real time with plasmonic nanoantennas. *Nat. Commun.* **4**, 2154 (2013).
16. Limaj, O. et al. Infrared Plasmonic Biosensor for Real-Time and Label-Free Monitoring of Lipid Membranes. *Nano Lett.* **16**, 1502-1508 (2016).
17. John-Herpin, A., Tittl, A. & Altug, H. Quantifying the Limits of Detection of Surface-Enhanced Infrared Spectroscopy with Grating Order-Coupled Nanogap Antennas. *ACS Photonics* **5**, 4117-4124 (2018).
18. Daniel Rodrigo, O.L., Davide Janner,Dordaneh Etezadi, F. Javier García de Abajo,Valerio Pruneri,Hatice Altug. Mid-infrared plasmonic biosensing with graphene. *Science* **349**, 165-168 (2015).
19. Lee, I.H. et al. Graphene acoustic plasmon resonator for ultrasensitive infrared spectroscopy. *Nat. Nanotech.* (2019).
20. Hu, H. et al. Far-field nanoscale infrared spectroscopy of vibrational fingerprints of molecules with graphene plasmons. *Nat. Commun.* **7**, 12334 (2016).

21. Yang, X. et al. Far-Field Spectroscopy and Near-Field Optical Imaging of Coupled Plasmon-Phonon Polaritons in 2D van der Waals Heterostructures. *Adv. Mater.* **28**, 2931-2938 (2016).
22. Hu, H. et al. Gas identification with graphene plasmons. *Nat. Commun.* **10**, 1131 (2019).
23. Hu, Y., López-Lorente, Á.I. & Mizaikoff, B. Versatile Analytical Platform Based on Graphene-Enhanced Infrared Attenuated Total Reflection Spectroscopy. *ACS Photonics* **5**, 2160-2167 (2018).
24. Zheng, B. et al. Graphene Plasmon-Enhanced IR Biosensing for in Situ Detection of Aqueous-Phase Molecules with an Attenuated Total Reflection Mode. *Anal. Chem.* **90**, 10786-10794 (2018).
25. Oh, S.-H. et al. Nanophotonic biosensors harnessing van der Waals materials. *Nat. Commun.* **12**, 3824 (2021).
26. Leenaerts, O., Partoens, B. & Peeters, F.M. Adsorption ofH2O,NH3, CO,NO2, and NO on graphene: A first-principles study. *Phys. Rev. B* **77**(2008).
27. Khaliji, K. et al. Plasmonic Gas Sensing with Graphene Nanoribbons. *Phys. Rev. Appl.* **13**, 011002 (2020).
28. Kulkarni, G.S., Reddy, K., Zhong, Z. & Fan, X. Graphene nanoelectronic heterodyne sensor for rapid and sensitive vapour detection. *Nat. Commun.* **5**, 4376 (2014).
29. Garoli, D., Yamazaki, H., Maccaferri, N. & Wanunu, M. Plasmonic Nanopores for Single-Molecule Detection and Manipulation: Toward Sequencing Applications. *Nano Lett.* **19**, 7553-7562 (2019).
30. Juan, M.L., Righini, M. & Quidant, R. Plasmon nano-optical tweezers. *Nat. Photon.* **5**, 349-356 (2011).
31. Maragò, O.M. et al. Optical trapping and manipulation of nanostructures. *Nat. Nanotech.* **8**, 807-819 (2013).
32. Barik, A. et al. Graphene-edge dielectrophoretic tweezers for trapping of biomolecules. *Nat. Commun.* **8**, 1867 (2017).
33. Freedman, K.J. et al. On-Demand Surface- and Tip-Enhanced Raman Spectroscopy Using Dielectrophoretic Trapping and Nanopore Sensing. *ACS Photonics* **3**, 1036-1044 (2016).
34. Freedman, K.J. et al. Nanopore sensing at ultra-low concentrations using single-molecule dielectrophoretic trapping. *Nat. Commun.* **7**, 10217 (2016).
35. Hu, H. et al. Gas identification with graphene plasmons. *Nat. Commun.* **10**, 1131 (2019).
36. Russo, C.J. & Passmore, L.A. Controlling protein adsorption on graphene for cryo-EM using low-energy hydrogen plasmas. *Nat. Methods* **11**, 649-652 (2014).
37. Ohno, Y., Maehashi, K., Yamashiro, Y. & Matsumoto, K. Electrolyte-Gated Graphene Field-Effect Transistors for Detecting pH and Protein Adsorption. *Nano Lett.* **9**, 3318-3322 (2009).
38. Yang, X. et al. Nanomaterial-Based Plasmon-Enhanced Infrared Spectroscopy. *Adv. Mater.* **30**, e1704896 (2018).
39. Neubrech, F. et al. Surface-Enhanced Infrared Spectroscopy Using Resonant Nanoantennas. *Chem Rev* **117**, 5110-5145 (2017).
40. Li, S. et al. Large transport gap modulation in graphene via electric-field-controlled reversible hydrogenation. *Nat. Electron.* **4**, 254-260 (2021).
41. Ahmadian Yazdi, A., Xu, J. & Berry, V. Phononics of Graphene Interfaced with Flowing Ionic Fluid: An Avenue for High Spatial Resolution Flow Sensor Applications. *ACS Nano* **15**, 6998-7005 (2021).

42. Jia, X. et al. Kinetic Ionic Permeation and Interfacial Doping of Supported Graphene. *Nano Lett.* **19**, 9029-9036 (2019).
43. Engen, J.R. et al. Developments in Hydrogen/Deuterium Exchange Mass Spectrometry. *Anal. Chem.* **93**, 567-582 (2021).
44. Atzrodt, J., Derdau, V., Kerr, W.J. & Reid, M. Deuterium- and Tritium-Labelled Compounds: Applications in the Life Sciences. *Angew. Chem. Int. Ed.* **57**, 1758-1784 (2018).
45. Masson, G.R. et al. Recommendations for performing, interpreting and reporting hydrogen deuterium exchange mass spectrometry (HDX-MS) experiments. *Nat. Methods* **16**, 595-602 (2019).
46. Loh Yong, Y. et al. Photoredox-catalyzed deuteration and tritiation of pharmaceutical compounds. *Science* **358**, 1182-1187 (2017).
47. Konermann, L., Pan, J. & Liu, Y.-H. Hydrogen exchange mass spectrometry for studying protein structure and dynamics. *Chem. Soc. Rev* **40**, 1224-1234 (2011).
48. Weiss, J.J. Nature of the Iron–Oxygen Bond in Oxyhæmoglobin. *Nature* **202**, 83-84 (1964).
49. Ordal, M.A. et al. Optical properties of the metals Al, Co, Cu, Au, Fe, Pb, Ni, Pd, Pt, Ag, Ti, and W in the infrared and far infrared. *Appl. Opt.* **22**, 1099-1119 (1983).
50. Rodrigo, D. et al. Double-layer graphene for enhanced tunable infrared plasmonics. *Light Sci. Appl.* **6**, e16277 (2017).

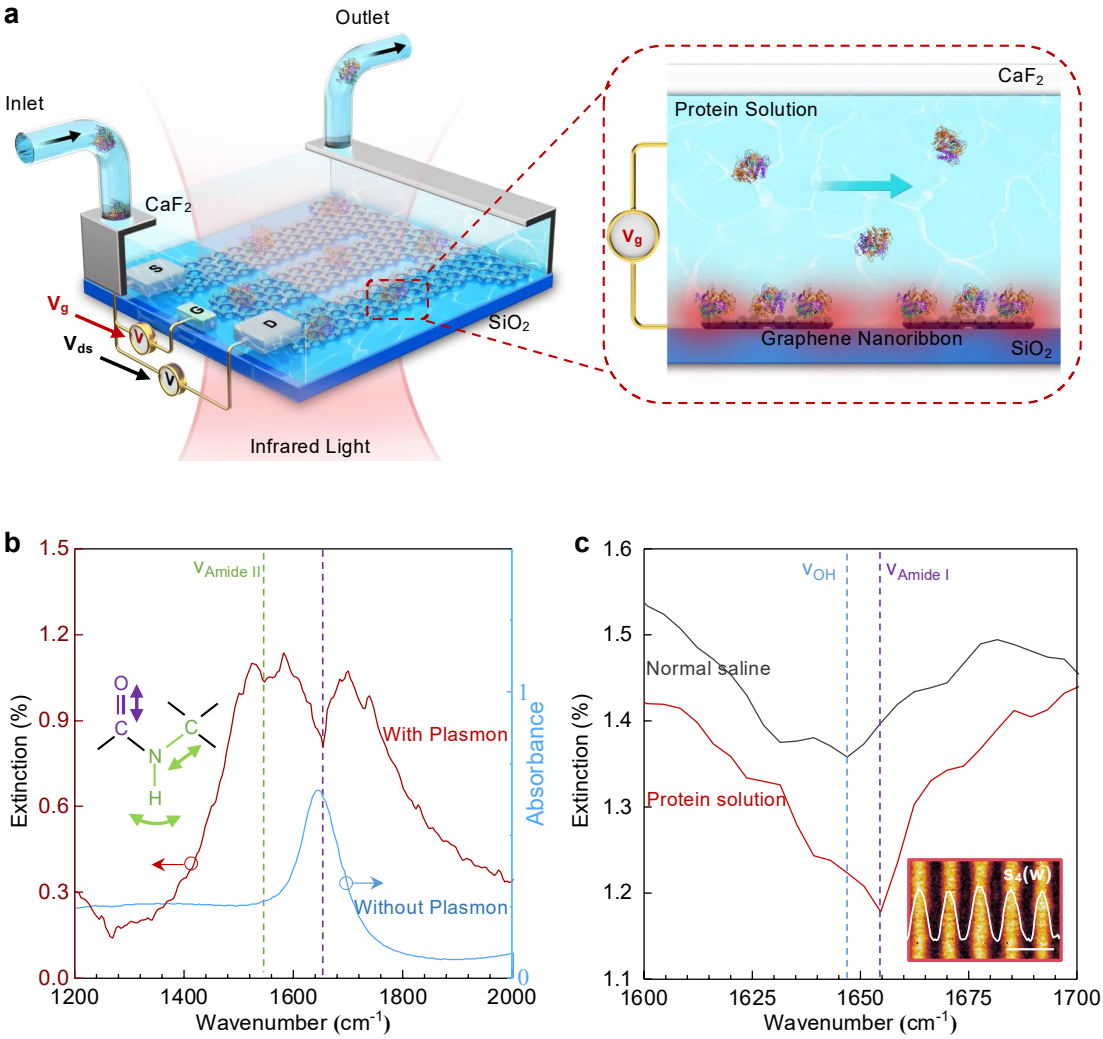

Figure 1. The tunable graphene plasmon-enhanced FTIR platform. (a) Schematic view of the tunable graphene plasmon-enhanced FTIR platform. **(b)** Transmission spectrum of protein solution (5 mg/mL) in the sensor cell with/without graphene plasmon enhancement. **(c)** The magnified mid-IR region (1600-1700 cm^{-1}) for graphene plasmon-enhanced FTIR before and after protein adsorption in the aqueous environment, E_F=-0.3 eV, graphene nanoribbon width is ~60 nm, the period is ~120 nm; Insert: The near-field optical image of p doped graphene nanoribbon at an IR wavelength of λ=10.526 μm (scale bar is 200 nm).

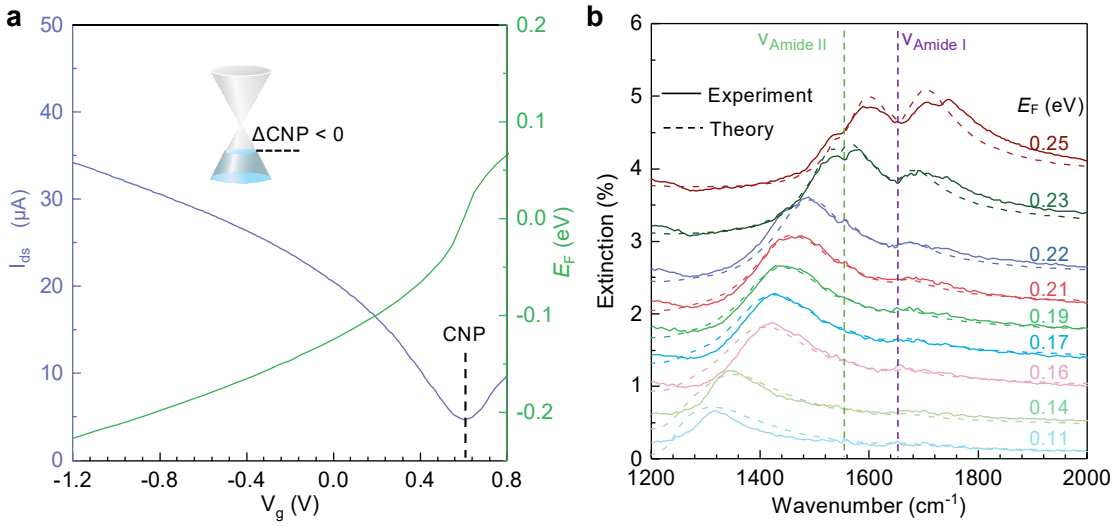

Figure 2: Tunable graphene plasmons via the effective gate voltage. (a) The transfer characteristic curve and the respective Fermi energy of the graphene plasmonic device after 1 mg/mL protein solution flows 2h, the graphene nanoribbon width is ~50 nm, and the period is ~100 nm. **(b)** The solid curves are experiment results of graphene plasmon response at different gate voltages, after 1 mg/mL protein solution flows 2h; The dashed curves are simulation results of graphene nanoribbon plasmon response are at different Fermi energies. The protein layer thickness is 8 nm, water thickness is 50 nm, graphene carrier mobility is set as 900 $cm^2/(V*s)$.

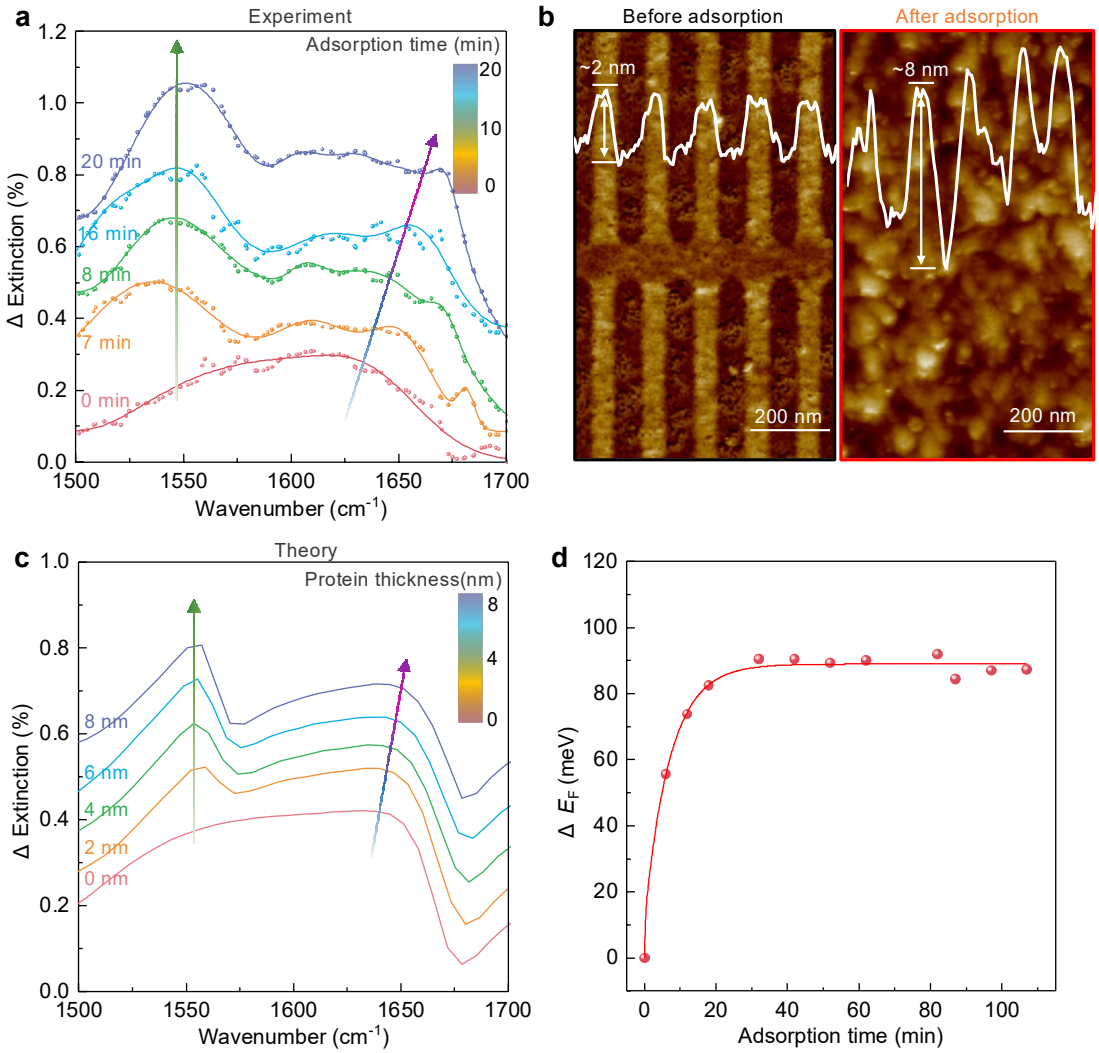

Figure 3: Protein adsorption and Graphene plasmons enhancement. (a) Plasmon-enhanced protein IR responses (ΔExtinction) at different adsorption times (0 min, 7 min, 8 min, 16 min, 20 min, graphene nanoribbon width is ~70 nm, the period is ~140 nm, and protein solution concentration is 5 mg/mL. **(b)** Morphologies and respective AFM height data of graphene nanoribbon before and after protein adsorption, scale bar is 200 nm. **(c)** Simulation results of graphene plasmon-enhanced protein IR spectrum with different adsorption thickness (0 nm, 2 nm, 4 nm, 6 nm, 8 nm), graphene nanoribbon width is 70 nm, the period is 140 nm, water thickness is 50 nm, graphene carrier mobility and Fermi energy are set as 900 $cm^2/(V*s)$ and -0.25 eV separately. **(d)** The CNP changes of the GP-aIR biosensor during protein adsorption in the physiological environment, extracted from Supplementary Fig. S2d.

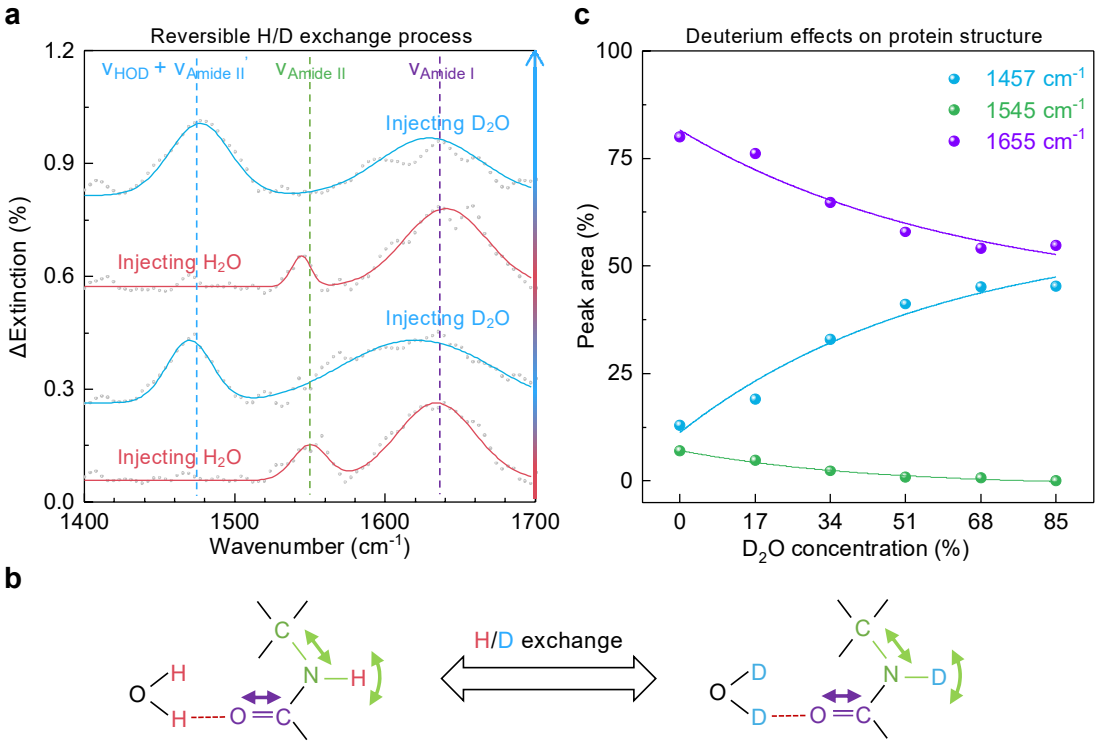

Figure 4: H/D exchange processes monitored by the graphene plasmonic sensor. **(a)** In-situ and real-time protein identification in H_2O and heavy water, the protein concentration is 1 mg/mL, graphene nanoribbon width is 60 nm, the period is 120 nm, E_F=-0.23 eV. The plasmon-enhanced protein responses (ΔExtinction) are extracted from Supplementary Fig. 7c. **(b)** The coupled peak area of protein and D_2O vibrational modes extracted from graphene plasmon-enhanced FTIR at different D_2O concentrations in Supplementary Fig. S7d. **(c)** Illustration of D_2O/H_2O induced molecular structure change and hydrogen bond interaction.